International Journal of Solids and Structures 321 (2025) 113567

Contents lists available at ScienceDirect

International Journal of Solids and Structures

journal homepage: www.elsevier.com/locate/ijsolstr

Efficient virtual element modeling of the bending failure in BCC lattice sandwich panels manufactured by L-PBF

Marco Lo Cascio, Gaetano Pollara, Dina Palmeri, Gianluca Buffa *, Alberto Milazzo, Livan Fratini

Department of Engineering, University of Palermo, Viale delle Scienze, Edificio 8, Palermo 90128, Italy

ARTICLE INFO

Keywords:
Virtual Element Method
Additive Manufacturing
Titanium Alloys
Lattice Structures

ABSTRACT

Lattice structures are gaining increasing interest in the aerospace field thanks to their promising applications. They can be used in metal sandwich panels as a core to reduce weight and provide additional functions to the structure. Laser Powder Bed Fusion (L-PBF) represents one of the best solutions to manufacture metal structures when high resolution is required. Finite element-based simulations of lattice structures' complex geometry require an extremely fine mesh, leading to prohibitively high computational costs and making the finite element model impractical for analysis. The Virtual Element Method (VEM) is a recently developed numerical technique that provides several advantages over the traditional finite element method. These advantages include the capability to manage complex geometries accurately, enhanced performance with distorted meshes, and increased flexibility in mesh generation. This paper introduces a novel and computationally efficient numerical approach that combines a non-linear Virtual Element Method formulation and equivalent two-dimensional modeling to predict the bending failure of Body-Centered Cubic (BCC) lattice sandwich panels fabricated via L-PBF. To validate and illustrate the effectiveness and potential of the proposed approach, numerical results are compared with experimental observations. For this purpose, a range of specimen configurations featuring different unit cell sizes and beam radius values were produced and tested. The findings reveal a strong alignment between the numerical predictions and experimental data and provide valuable insights into the failure mechanisms involved.

1. Introduction

Lattice (or cellular) materials are a type of metamaterial consisting of a periodic network of structural elements such as beams or membranes (Gibson and Ashby, 1997). Due to their complex geometry, it is almost impossible to build lattice structures with traditional manufacturing methods (Benedetti et al., 2021). In this frame, Additive Manufacturing (AM) can play a fundamental role thanks to its layer-by-layer fabrication and freedom of design, thus allowing part consolidation, manufacture of lightweight components, low buy-to-fly ratios (between 1:1 and 3:1), and a reduction of lead time (Blakey-Milner et al., 2021). Among the AM technologies, laser powder bed fusion (L-PBF) can be adopted in the case of metallic materials and when high resolution is required (DebRoy et al., 2018). During the process, the powder bed is spread along the build plate, and a laser beam melts the powder selectively according to the slicing le. After that, the platform is lowered by the assigned layer thickness, and the process continues until the part is completed (Vock et al., 2019). For aerospace applications, where high mechanical properties and corrosion resistance are needed, Ti-6Al-4V metallic powder is usually employed (Buffa et al., 2024). Lattice structures can be grouped into three main classes: a) strut-based, b) skeletal Triply Periodic Minimal Surfaces (TPMS), and c) sheet-TPMS. The first class consists of a repetition of a unit cell structure characterized by struts (or beams) and nodes. The other classes are built according to a mathematical function that divides the space into two or more interlocked domains by locally minimizing the surface area for a given boundary, resulting in single connected domains with no enfolded voids (Al-Ketan et al., 2018). Recently, an increased interest in strut-based Body-Centered Cubic (BCC) lattice structures has been reported in the literature for aerospace applications. In detail, these structures can be used as a core of metal sandwich panels to provide high stiffness, low-density structure, great internal thermal exchange surface, and energy absorption capacity (Wu

* Corresponding author.
E-mail address: gianluca.buffa@unipa.it (G. Buffa).

https://doi.org/10.1016/j.ijsolstr.2025.113567
Received 7 May 2025; Received in revised form 28 June 2025; Accepted 10 July 2025
Available online 12 July 2025

et al., 2018; Georges et al., 2022). The idea is to manufacture multi-functional panels integrating anti-ice systems within the primary structure, instead of using multiple components added to the primary structure through joining techniques such as welding, bolts, or rivets. These panels are characterized by the following design variables: cell type, cell size, beam radius, and shell thickness (Bici et al., 2018). In the literature, several studies are focusing on the mechanical behavior of such sandwich panels using different materials and lattice cells. Numerical models are often employed to predict the mechanical response of metallic lattice sandwich panels. Acanfora et al. (Acanfora et al., 2021) investigated metallic sandwich panels with lattice core structures for shock-absorbing systems. In particular, a numerical model has been developed to understand the influence of the main lattice geometrical parameters on the energy absorption capacity. The behavior of AM Auxetic honeycomb sandwich panels (AHSP) made of Ti-6Al-4V under blast load conditions was studied by Wei et al. (Wei et al., 2023). A computational model was developed to provide insight into the crack propagation, dynamic deflection, pressure wave evolution, and energy absorption of AHSP. Kang et al. (Kang et al., 2019) analyzed the behavior of stainless-steel multi-lattice sandwich panels during three-point bending tests. The study focused on the topology optimization of the lattice core structures in order to obtain the best compromise in terms of mechanical resistance and mass density. The quasi-static compressive response of AlSi10Mg BCCZ lattice sandwich panel has been addressed by Li et al. (Li et al., 2018) through a Finite Element Analysis (FEA). The numerical model was developed to predict the compressive modulus and initial crushing strength of multi-layer lattice panels.

Various conventional finite element discretizations can effectively model the behavior of strut-based lattice structures, and the selection of a specific element type significantly affects the results of simulations (Smith et al., 2013). Both beam and continuum elements have been used to simulate the mechanical behavior of lattice structures. For low-volume fractions and moderate to high strut slenderness, beam/rod-type elements based on Eulero-Bernoulli beam theory or shear-deformable Timoshenko beam theory may be appropriate (Červinek et al., 2022). At higher volume fractions, theoretical and computational analyses based on beam theory may become inapplicable due to the increased thickness of the struts as well as the effect of the nodes where the struts intersect. Using beam elements generally lowers computational costs, whereas three-dimensional continuum elements can provide more detailed information about the stress and strain distribution (Imbalzano et al., 2017), making them the preferred choice for modeling the fracture and failure behavior of lattice structures (Wei et al., 2020).

Three-dimensional finite element simulations require significant computational resources, making them quite expensive in terms of processing time and power. Finite element models of low-volume fraction lattice structures with multiple high aspect ratio struts require a fine three-dimensional mesh. This results in a substantial number of degrees of freedom (Lozanovski et al., 2019). Consequently, simulating large low-volume fraction lattice structures can require such extensive computational resources that it limits the ability to perform mesh convergence studies or may even render finite element models infeasible. As a result, it is often necessary to reduce the model size by adopting discretization based on less-performing beam elements (Luxner et al., 2005).

The reduction of computational costs in three-dimensional finite element simulations of lattice structures is a significant challenge. To effectively decrease simulation time while still providing meaningful insights and sufficient reliability during preliminary analyses, equivalent two-dimensional finite element models can be employed. While it is relatively straightforward to create a two-dimensional model of the lattice structure for so-called two-dimensional lattice configurations (e.g., triangular, kagome, hexagonal) (Seiler et al., 2019), the process is more complex for three-dimensional truss-based lattice configurations (e.g., BCC, Octet Truss) and any attempt at such simplified modeling must be carried out considering the effect of the three-dimensional configuration on the structure's mechanical behavior.

Another key challenge in finite element modeling of materials with complex geometries, such as lattice structures, is the automatic generation of a mesh that can conform to the intricate features of the computational representation of the material structural topology. This mesh must produce accurate results while also maintaining a reasonable computational cost. Automatic meshers that use standard finite elements may run into problems in creating a conformal mesh, generating, in some regions of the domain with particularly complex geometry, elements with excessive distortions whose presence affects the numerical accuracy. A more refined mesh can overcome this issue, but it will involve higher computational costs. A finer mesh can mitigate this issue, but at an increased computational cost. Even when the automatic mesh generation process does not create degenerated elements with coarse meshes, a localized mesh refinement may be necessary to ensure the accuracy of the results in some areas of the computational domain. For lattice materials modeled with two- or three-dimensional elements, this means, for instance, placing enough elements across the thickness of a beam of the unit cell or enough elements to capture the stress concentrations at the beam joints. Therefore, generating an optimal mesh in a completely automatic way is often inefficient and requires considerable time-consuming effort on the part of an operator.

The Finite Element Method (FEM) is widely considered the leading technique for the numerical approximation of partial differential equations in structural and continuum mechanics. The core of the FEM's formulation is the use of polynomial basis functions defined on simple geometric elements such as triangles and quadrilaterals in two dimensions or tetrahedra and hexahedra in three dimensions. The success of the FEM can be attributed to a strong theoretical foundation and a long history of practical applications spanning several decades. However, while the FEM has proven to be highly effective, it does exhibit limitations when dealing with highly irregular meshes, distorted elements, or complex geometries where conforming mesh generation becomes difficult or computationally expensive.

The Virtual Element Method (Beirão Da Veiga et al., 2013) (VEM) is a numerical technique recently introduced as a generalization of the FEM. In the VEM, the construction of the approximation spaces relies on shape functions that are not explicitly defined in closed form but are instead defined implicitly through their degrees of freedom and projection operators. This approach allows the VEM to seamlessly handle elements of arbitrary geometry. By removing the geometric constraints on element shapes that are characteristic of the FEM, it has been demonstrated (Lo Cascio et al., 2021) that the VEM significantly simplifies the mesh generation process and offers greater flexibility in creating meshes for complex domains. Another key advantages of the VEM with respect to the FEM is its insensitivity to mesh quality. While the accuracy and convergence of FEM solutions can degrade significantly because of poor mesh quality, the VEM has proved (Lo Cascio et al., 2019) to maintains its performance even in the presence of highly irregular elements. This robustness stems from its formulation, which enforces polynomial consistency and stability independently of element shape.

Although the VEM has been successfully applied in modeling the behavior of composite (Lo Cascio et al., 2021; Lo Cascio et al., 2019) and other materials having a complex microstructure (Marino et al., 2019; Böhm et al., 2023), its applicability to lattice sandwich panels has yet to be proven. It is worth remarking that the macro-scale geometrical complexity inherent in beam-like structures, characterized by large void volume fractions and several stress concentration areas, adds difficulties in the proper prediction of the structure's behavior.

This study focuses on experimental and numerical investigations of the deformation and failure of additively manufactured Ti 6Al 4V BBC lattice sandwich panels subjected to three-point bending loads. A novel and computationally efficient numerical approach is presented, which combines a non-linear VEM based on a non-local isotropic damage model and an equivalent two-dimensional modeling technique. To

validate the proposed modeling approach, experimental measurements were conducted. A range of specimen configurations, featuring different unit cell sizes and beam radius values, was produced and tested. The results show a strong agreement between the numerical predictions and the experimental data and provide valuable insights into the influence of the lattice micro-architecture, namely, beam radius and cell size, on the ultimate strength and failure behavior.

The remainder of this paper is organized as follows. Section 2 describes the design and fabrication of the lattice sandwich panels and the experimental setup used for the bending tests. Section 3 presents the numerical modeling approach, detailing the VEM formulation and the development of equivalent two-dimensional models. Section 4 reports and compares experimental and numerical results. Section 5 discusses the key findings, including insights into the mechanical behavior and computational efficiency of the proposed approach. Finally, Section 6 summarizes the main conclusions and outlines potential directions for future work.

2. Fabrication and experiments

2.1. Sample design and manufacturing

Sandwich panels made of a BCC lattice structure as a core and two fully dense shells (Fig. 1a) were fabricated as a unique part by Laser Powder Bed Fusion (L-PBF). The main geometrical parameters of the BCC unit cell, such as cell size (L) and beam radius (R), are represented in Fig. 1b.

In order to investigate the effect of the above-mentioned geometrical features on the mechanical behavior of the sandwich panels, two different unit cell dimensions, C2 and C4, were tested. In detail, C2 and C4 correspond to $L = 2$ mm and $L = 4$ mm, respectively. Three different beam radii were selected for each unit cell to obtain cells with a volume fraction (V_f), i.e. the volume occupied by the lattice within the cell V_l divided by the volume of the parent solid (V_s, volume of the unit cell being considered), of 0.264, 0.358, and 0.457. Samples were identified according to the cell size and beam radius used, as specified in Table 1. Thus, a sandwich lattice panel fabricated with an $L = 2$ mm and $R = 0.25$ mm is designated as C2-R0.25.

In this way, six different cells were obtained, resulting in six different sandwich panels (see Table 1). All the geometries were designed with Autodesk Fusion 360 and imported into Magics Materialize software to create the support structures and assign the process parameters for the printing process. Samples were printed with an SLM280HL machine using Ti-6Al-4V spherical powder with a Gaussian distribution of 20–63 μm and mass density $\rho = 4.43$ g/cm^3. The build chamber was filled with Argon to lower the oxygen level to 0.1 %, while the build platform was preheated up to 200°C to reduce thermal gradients and residual stress (Palmeri et al., 2023). The process parameters were kept constant for

Table 1
Design variables adopted in this study.

Sample ID	L (mm)	R (mm)	V_f	Unit cell	Lattice sandwich panel
C2-R0.25	2	0.25	0.264		
C2-R0.30	2	0.30	0.358		
C2-R0.35	2	0.35	0.457		
C4-R0.50	4	0.50	0.264		
C4-R0.60	4	0.60	0.358		
C4-R0.70	4	0.70	0.457		

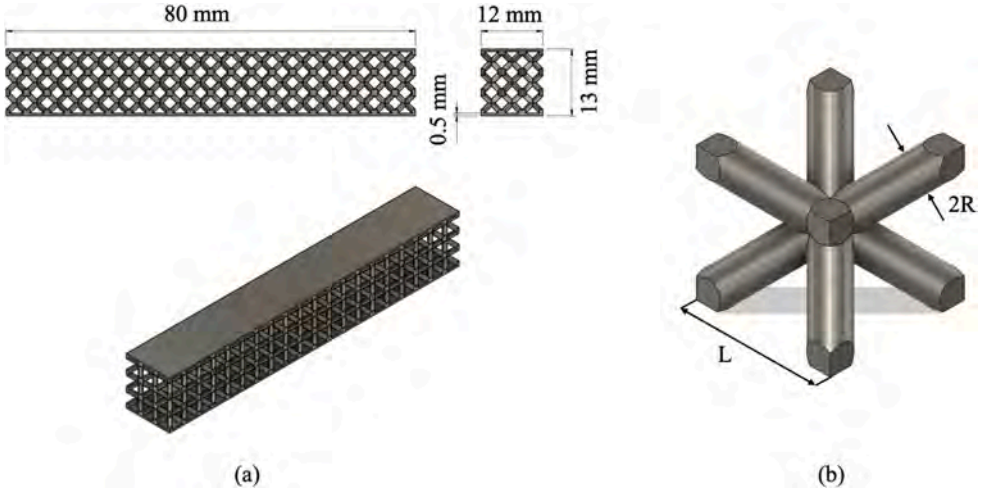

Fig. 1. (a) Sketch of the sandwich panel with unit cell C4 and beam radius $R = 0.50$ mm, (b) BCC unit cell geometrical parameters (L: cell size, R: beam radius).

each geometry. Particularly, the main process parameters are listed as follows: laser power of 350 W, scan speed of 1400 mm/s, hatch distance of 120 μm, and layer thickness of 30 μm. All samples were fabricated with a build orientation equal to 90° to minimize support structures and reduce distortions (Fig. 2).

2.2. Experimental tests

Sandwich panels were designed according to ASTM E290 for three-point bending tests (Astm, 2014). The dimensions used for all the samples (80 mm x 12 mm x 13 mm) are shown in Fig. 1. For each sample, the lattice section was 12 mm x 12 mm, while the shell thickness was set equal to 0.5 mm. Metal lattice sandwich panels are lightweight structural components primarily designed for aerospace applications, where their performance under bending is often critical. This is due to the unique loading conditions these structures encounter in aerospace environments, where bending stresses generated by the distribution of aerodynamic forces tend to dominate. Consequently, to better understand and characterize the mechanical properties of metal lattice sandwich panels, three-point bending tests were chosen. This test configuration allows for a more accurate assessment of the material's response to ensure the reliability and efficiency of metal lattice sandwich panels in real-world aerospace applications. Three-point bending tests were performed on a Galdabini Quasar 600 universal testing machine. The testing setup is shown in Fig. 3. For each unit cell configuration, $n = 3$ specimens were tested, and load–displacement data were measured. Tests were conducted at a constant velocity of 0.5 mm/min. Fracture surface analyses were carried out with a Phenom ProX Desktop SEM to understand the failure mechanism of metal lattice sandwich panels during three-point bending tests.

3. Numerical modeling

In this study, the computational analyses aim to determine two-dimensional modeling equivalent to experimental tests to characterize the collapse mechanism of sandwich panels with BCC lattice cores subjected to bending loads. The numerical simulations have been performed using the Virtual Element Method (VEM) implemented on an in-house developed code. In this Section, the first-order non-linear VEM formulation utilized for modeling progressive damage and failure is briefly recalled, and details of the numerical models are provided.

3.1. Virtual element formulation for non-local isotropic damage

The computational domain is partitioned into a finite set Ω_h of non-overlapping polygonal elements E of arbitrary shape and number of edges along the boundary ∂E. On each element, the local set of discrete equilibrium equations is obtained from the principle of virtual displacements, which reads

$$\int_E \delta\boldsymbol{\varepsilon}^\intercal \, \sigma \, dE = \int_E \delta\boldsymbol{u}^\intercal \, b \, dE + \int_{\partial E} \delta\boldsymbol{u}^\intercal \, t \, ds \tag{1}$$

here, $\delta\boldsymbol{u}$ are any arbitrary, kinematically admissible displacements, $\delta\boldsymbol{\varepsilon}$ is the strain tensor stemming from $\delta\boldsymbol{u}$, $\boldsymbol{\sigma}$ is the stress tensor (all tensors are in Voigt form), $\boldsymbol{b}$ is the body force vector, $\boldsymbol{t}$ is the vector of boundary tractions. The degrees of freedom of each element are the values of the displacement components at each of its n_v vertex v, collected into the vector $\boldsymbol{d}_E$. The displacement field $\boldsymbol{u}$ within the element is approximated as

$$u = \boldsymbol{N}_E \boldsymbol{d}_E \tag{2}$$

The matrix $\boldsymbol{N}_E$ comprises the virtual shape functions N_v associated with each vertex v. These functions are globally continuous linear polynomials defined along the edges of the element. However, their specific form is unknown within the element, which means that an expression for the strains $\boldsymbol{\varepsilon}$ cannot be obtained by differentiation of the shape functions.

Therefore, a projection operator is introduced, defined by the orthogonality condition so that the error induced by using an approximated strain tensor $\boldsymbol{\varepsilon}_\pi$ instead of $\boldsymbol{\varepsilon}$ has no components along the space of any constant polynomial $\boldsymbol{p}$.

$$\int_E \boldsymbol{p}^\intercal \, (\boldsymbol{\varepsilon}_\pi - \boldsymbol{\varepsilon}) \, dE = 0 \tag{3}$$

Having $\boldsymbol{p}$ and $\boldsymbol{\varepsilon}_\pi$ constant components, and using Gauss's theorem to switch the integration to the boundary of the element, the tensor of the projected strain $\boldsymbol{\varepsilon}_\pi$ can be written as

$$\boldsymbol{\varepsilon}_\pi = \boldsymbol{\Pi}_E \boldsymbol{d}_E \tag{4}$$

where $\boldsymbol{\Pi}_E$ denotes the matrix representation of the projector

$$\boldsymbol{\Pi}_E = \frac{1}{A_E} \sum_{e=1}^{n_e} \int_e \boldsymbol{n}_e \boldsymbol{N}_E ds, \boldsymbol{n}_e = \begin{bmatrix} n_x & 0 & n_y \\ 0 & n_y & n_x \end{bmatrix}^\intercal \tag{5}$$

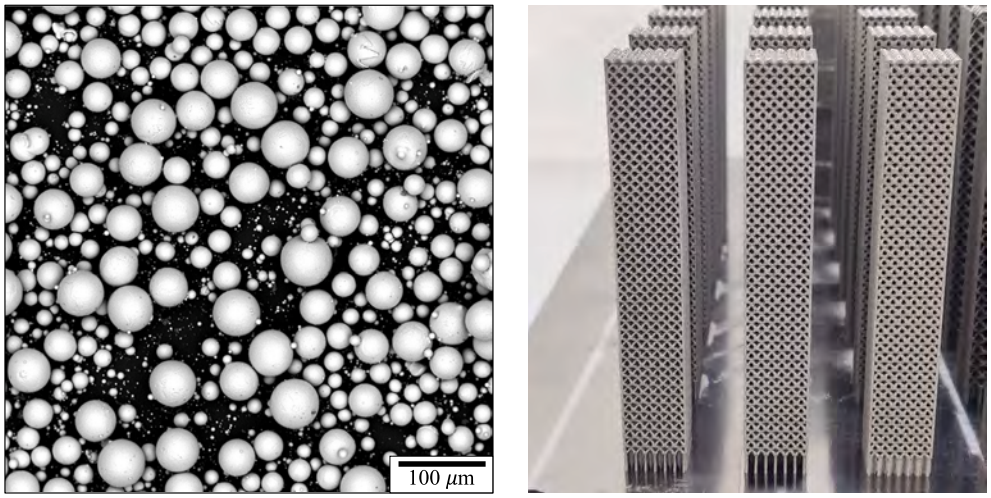

Fig. 2. L-PBF of Ti-6Al-4V lattice sandwich panels: (a) SEM images of the used powder, (b) Printed C2 lattice sandwich panels with support structures.

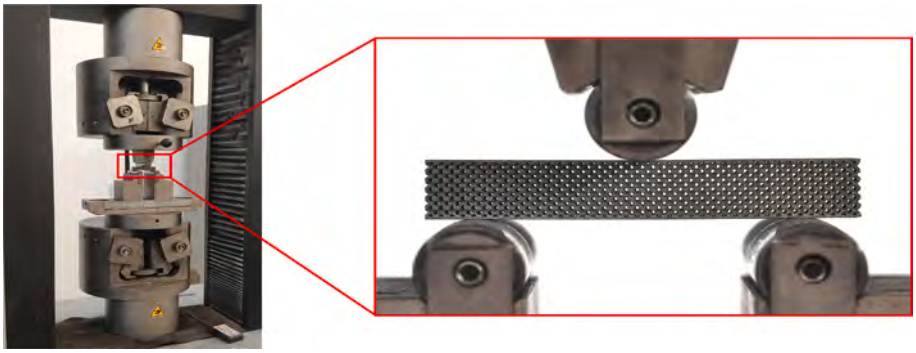

Fig. 3. Testing machine overview of the three-point bending test setup.

where A_E is the area of the polygonal element E, bounded by its n_e edges e and $\boldsymbol{n}_e$ is the matrix containing the components n_x and n_y of the outward unit normal vector over each edge e. The right-hand side of Eq. (5) can be computed because the restriction of the virtual shape functions N_v along the edges are, by definition, known piecewise linear polynomials. For a generic element E, the stiffness matrix is given as the sum of two terms

$$\boldsymbol{K}_E = A_E \boldsymbol{\Pi}_E^{\mathrm{I}} \boldsymbol{C} \boldsymbol{\Pi}_E + \boldsymbol{K}_E^{\mathrm{s}} \tag{6}$$

The first term in Eq. (6), which stems from the discrete form of the virtual strain energy stored within the element and depends on the tangent material stiffness tensor $\boldsymbol{C}$, is the contribution from the constant polynomial projection of the strain field. It is computed from Eq. (1) by employing the virtual element approximation in Eq. (4) and noting that the integrand is constant over the element E. The second term, $\boldsymbol{K}_E^{\mathrm{s}}$ is a stabilization term that must be incorporated into the stiffness matrix to prevent the occurrence of spurious zero-energy modes. There are various definitions of this term in the literature. In this case, it has been computed as described by Beirao da Veiga et al. (Beirão Da Veiga et al., 2013). Although the detailed expression is omitted here for the sake of brevity, the interested reader is referred to Lo Cascio et al. (Lo Cascio et al., 2021) and the references cited therein. The equivalent nodal forces $\boldsymbol{F}_E$ resulting from the work of external loads can be computed as

$$\boldsymbol{F}_E = \int_{\partial E} \boldsymbol{N}_E^{\mathrm{I}} t b \, ds + \sum_{i=1}^{n_v} w_i b(v_i) \tag{7}$$

The first term on the RHS is the contribution of the boundary tractions, and it is directly computable since the virtual shape functions $\boldsymbol{N}_E$ are known linear polynomials over the element boundary ∂E. The second term comes from the work of the body forces and can be computed using a vertex-based quadrature rule with weights w_v chosen to provide the exact integral on E when applied to linear functions (da Veiga et al., 2013). The elemental equilibrium equation is

$$\boldsymbol{K}_E \boldsymbol{d}_E = \boldsymbol{F}_E \tag{8}$$

Once the elemental matrices are computed, the overall structural problem can be addressed by employing standard finite element numbering, assembly, and solution procedures; the equation for solving the discretized system reads

$$K d = F \tag{9}$$

where $\boldsymbol{K}$ is the structural system stiffness matrix, $\boldsymbol{F}$ is the system nodal force vector, and $\boldsymbol{d}$ is the vector of the displacement components of each node.

The equations for the isotropic damage model, which is used to describe the failure of the material, are defined as follows (Simo and Ju, 1987)

$$\sigma = (1 - \omega) \boldsymbol{C}^0 \boldsymbol{\varepsilon}_{\boldsymbol{\pi}} \tag{10}$$

where $\boldsymbol{C}^0$ is the material stiffness tensor for the pristine elastic material. The scalar damage variable ω measures the reduction in the material's stiffness. Its allowable range is $0 \leq \omega \leq 1$. Specifically, $\omega = 0$ indicates that the material is in pristine condition, while $\omega = 1$ represents a fully degraded state. Damage growth is activated upon fulfillment of the condition

$$F = \tau - \kappa = 0, \kappa = \max_{\lambda \in \mathscr{H}} \{\tau(\lambda)\} \tag{11}$$

where τ is a norm of the strains used to determine if the considered stress state belongs to the elastic domain, when $F < 0$, or if it induces damage initiation or evolution, $F = 0$. The monotonically increasing internal variable κ represents the damage threshold at the current loading step λ, which is a function of the loading history $\mathscr{H}$. The expression adopted for the equivalent strain is (de Vree et al., 1995)

$$\tau = \frac{k-1}{2k(1-2\nu)} I_1 + \frac{1}{2k} \sqrt{\left(\frac{k-1}{1-2\nu} I_1\right)^2 + \frac{12k}{(1+\nu)^2} J_2} \tag{12}$$

with I_1 first invariant of the strain tensor, J_2 the second invariant of the deviatoric strain tensor, ν the Poisson's ratio, and k the ratio of the uniaxial compressive strength f_c and the uniaxial tensile strength f_t of the considered material (here f_c is assumed twice f_t).

The damage variable ω is linked to the internal variable κ by the linear softening damage evolution law defined as (Jirásek, 2007)

$$\omega(\kappa) = \frac{\kappa_f}{\kappa_f - \kappa_0} \left(1 - \frac{\kappa_0}{\kappa}\right) \tag{13}$$

where the parameter κ_0 identifies the damage initiation condition that can be inferred from the stress–strain diagram under uniaxial tension, depending on the expression chosen for the equivalent strains. The parameter κ_f controls the softening response behavior. In order to use an incremental-iterative solver, the tangent material stiffness tensor $\boldsymbol{C} = \frac{\partial \sigma}{\partial \varepsilon_\pi}$ at a certain loading step λ is derived by linearization of the non-linear constitutive law in Eq. (10).

To help address mesh sensitivity issues, an integral-type non-local regularization approach (Pijaudier-Cabot and Bažant, 1987) is employed, which consists of replacing the local value of the equivalent strain $\tau(\boldsymbol{x}_p)$ at a certain point $\boldsymbol{x}_p$ with its weighted average

$$\bar{\tau}(\mathbf{x}_p) = \int_{\Omega_h} \alpha(\mathbf{x}_p, \mathbf{x}_q) \tau(\mathbf{x}_q) d\Omega \tag{14}$$

where α is a non-local weight function of the distance $r = ||\mathbf{x}_p - \mathbf{x}_q||$ between two considered material points defined as

$$\alpha(\mathbf{x}_p, \mathbf{x}_q) = \frac{\alpha_0(r)}{\int_{\Omega_h} \alpha_0(r) d\Omega} \tag{15}$$

The nonnegative function α_0 also depends on the prescribed value of the interaction radius r, and it is chosen as

$$\alpha_0(r) = \langle 1 - \frac{r^2}{\bar{r}^2} \rangle^2 \tag{16}$$

With the present virtual element formulation, each mesh element has a uniform strain field, and no integration weight exists. Thus, the computation of the integral over the circular domain is performed by assuming the centroid of each element as the evaluation point and the area of the considered element as the corresponding weight.

3.2. Numerical model

Besides the considered material, the mechanical properties and response of strut-based lattice materials are significantly influenced by microstructural parameters such as the lattice topology and volume fraction (Ashby, 2006).

In order to develop a two-dimensional numerical model that accurately simulates the mechanical behavior of a strut-based lattice with a three-dimensional configuration, the influence of the three-dimensional arrangement on the mechanical response of the structure is investigated.

The two-dimensional projection of the BCC lattice can be associated with a square honeycomb lattice (Li et al., 2018) having cell walls oriented along the ± 45° directions. Models of such a square honeycomb lattice and its unit cell are shown in Fig. 4.

An important distinction in lattice structures is between a bending-dominated and a stretching-dominated structure, and both BCC lattice and square honeycomb unit cells are bending-dominated structures (Deshpande et al., 2001; Zhong et al., 2023). The second moment of area I is the geometric parameter that governs the bending stiffness of a beam. For a round cross-section, such the one of the BCC beams, it can be computed as

$$I = \frac{\pi t^4}{64} \tag{17}$$

For the rectangular cross-section of a wall of the square honeycomb unit cell, the second moment of area with respect to the out-of-plane axis is

$$I = \frac{Lt^3}{12} \tag{18}$$

By imposing that a square honeycomb unit cell wall has the exact second moment of area of two beams of a BCC unit cell, a preliminary estimate of the values of the equivalent half-thickness R_e is calculated. These values are listed in Table 2. The values of R_e effectively used in the numerical simulations are slightly different and are listed in Table 3.

To further reduce computational costs, the TPB test's symmetry in terms of geometry, constraint, and load conditions was exploited by analyzing a model consisting of only the left half of the specimen, as shown in Fig. 5. Each model was discretized using a structured mesh of quadrangular VEM elements for the skin and generic VEM polygonal elements for the core lattice.

The VEM offers greater flexibility in mesh generation compared to the standard FEM, allowing for the independent application of optimal mesh densities across different regions of the computational domain. For example, the skin and core regions can be meshed with different mesh sizes and seamlessly connected. Additionally, local mesh refinement can be implemented in specific areas, such as portions of the lattice core, with the remeshing process affecting only the chosen regions.

In this application, a local mesh refinement was applied, as illustrated in Fig. 5, to the right side of the half-specimen. The refinement technique used is called Polytree, which recursively subdivides a polygonal element with n edges into n + 1 new polygonal elements. This approach results in the creation of hanging nodes at the boundaries between two mesh areas with different refinement levels, leading to a non-conformal mesh from a standard FEM perspective. However, the VEM can accommodate elements with arbitrary shapes and an arbitrary

Table 2
Equivalent half-thickness R_e of the walls of the two-dimensional lattices computed using the second moment of area (I) of the beams of the manufactured specimen.

Sample ID	L (mm)	R (mm)	I (mm^4)	R_e (mm)
C2-R0.25	2	0.25	0.00614	0.08
C2-R0.30	2	0.30	0.01272	0.10
C2-R0.35	2	0.35	0.02357	0.13
C4-R0.50	4	0.50	0.09818	0.16
C4-R0.60	4	0.60	0.20358	0.21
C4-R0.70	4	0.70	0.37715	0.26

Table 3
Geometric properties of the square honeycomb unit cells used in the numerical simulations.

Sample ID	Unit cell length L (mm)	Equivalent half-thickness R_e (mm)
C2-R0.25	2	0.070
C2-R0.30	2	0.095
C2-R0.35	2	0.105
C4-R0.50	4	0.150
C4-R0.60	4	0.200
C4-R0.70	4	0.250

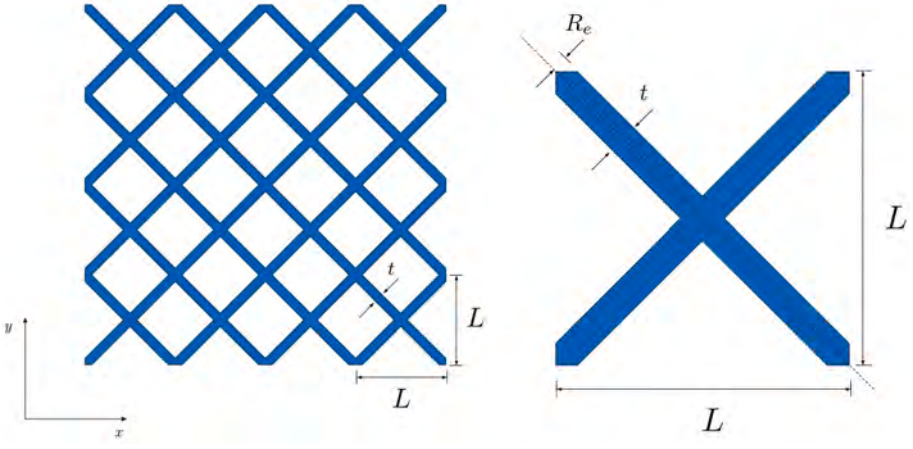

Fig. 4. Two-dimensional model of (a) square honeycomb lattice, (b) square honeycomb unit cell.

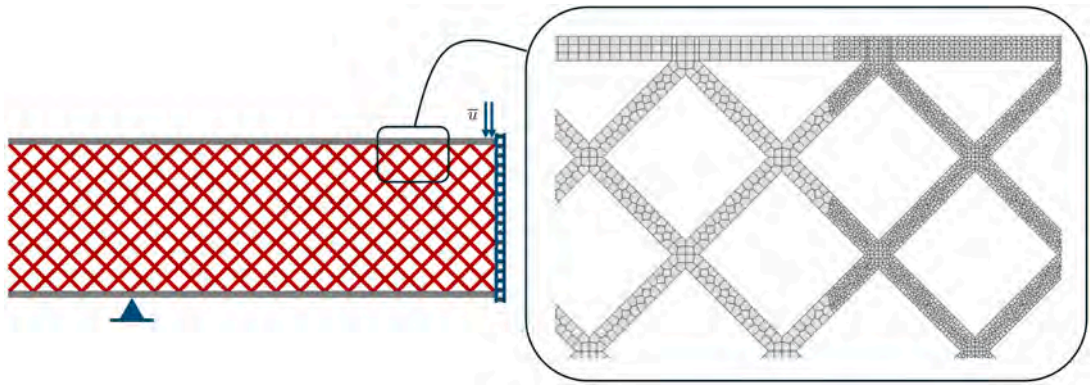

Fig. 5. Computational model for the Three-Point Bending (TPB) test with details of the polygonal mesh and the local mesh-refinement strategy.

number of edges, allowing it to integrate the hanging nodes into the connectivity of the non-refined elements, resulting in a VEM-conformal mesh. Further details regarding this procedure can be found in the work of Lo Cascio et al. (Lo Cascio et al., 2020). The local mesh refinement significantly reduces the total computational cost compared to using uniformly fine meshes or traditional mesh refinement approaches. A mesh convergence analysis was carried out for each virtual specimen to ensure the reliability and accuracy of the numerical model predictions. Table 4 details the average mesh size (h_{avg}) and the number of degrees of freedom (DOF) for each virtual specimen. It was observed that simulations with a finer mesh resulted in only a marginal improvement in prediction accuracy. Constraints were applied to prevent the horizontal displacement of the mesh nodes placed at the far right of the model and the vertical displacement of the node corresponding to the left support. The vertical load was generated by imposing prescribed vertical (negative) displacement on the nodes lying on the upper edge of the upper skin within 1 mm of the far-right side of the model. A very small *non-damage zone* (height 1.2 mm, width 2 mm) has been set close to the support zone to prevent spurious stress concentrations. This is incorporated into the model algorithm by assigning a pure elastic (no degradation) material model for the mesh elements in this zone. The constitutive model adopted for the Ti-6Al-4V alloy is based on the non-local isotropic damage model described in Section 3.1. The values for the Young's modulus, the Poisson's ratio and the ultimate tensile strength are listed in Table 5. The uniaxial compressive strength has been assumed to be twice that of the tensile one. The parameters governing the linear softening damage evolution law have been derived, according

Table 5
Ti 6Al 4V alloy material properties used in numerical simulations.

Young's modulus	Poisson's ratio	Ultimate tensile strength
109.1 GPa (Bartsch et al., 2021)	0.29 (Bartsch et al., 2021)	950 MPa (Palmeri et al., 2022)

Table 4
Mesh data for the virtual specimens.

Sample ID	L (mm)	R_e (mm)	V_f	h_{avg} (mm)	DOF	
C2-R0.25	2	0.070	0.188	0.085	132,194	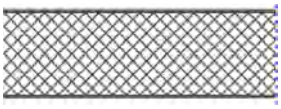
C2-R0.30	2	0.095	0.251	0.151	50,570	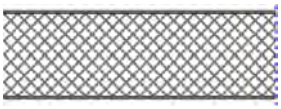
C2-R0.35	2	0.105	0.275	0.163	46,090	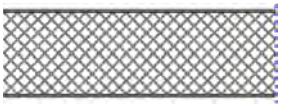
C4-R0.50	4	0.150	0.201	0.159	31,624	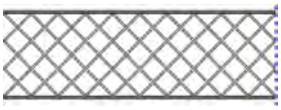
C4-R0.60	4	0.200	0.263	0.185	29,416	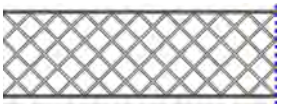
C4-R0.70	4	0.250	0.322	0.143	68,660	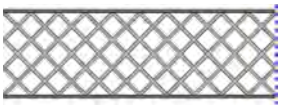

to the chosen form of the equivalent strain, from uniaxial tensile test data, considering the assumed predominantly brittle failure behaviour of the material. Plane strain assumptions have been used. Simulations have been carried out under displacement control using a modified Newton-Raphson iterative solution method.

4. Results

4.1. Experimental results

In order to validate the numerical model, bending tests were carried out on the lattice sandwich panels fabricated via L-PBF. Overall, the experiments have shown a brittle fracture behavior of the sandwich panel lattice. In Figs. 6 and 7, the results in terms of load and displacement are shown for fixed unit cells and different beam radii. Fig. 6 illustrates only the load–displacement curves for the C2 lattice sandwich panels. In this way, it is easy to highlight the beam radius's influence on the mechanical properties of these structures. In detail, it can be observed how the mechanical strength of the panels increases by increasing the beam radius. Moreover, lower displacements are allowed. A similar trend was observed for the C4 unit cells (Fig. 7). However, the load–displacement curves indicate that C4 cells exhibit a more brittle behavior compared to C2 cells. It is worth noticing that, by comparing the curves for a fixed beam radius, a lattice sandwich panel with a smaller cell size can withstand higher displacements and loads.

Table 6 presents the results of the three-point bending tests in terms of force and displacement. The mean values and standard deviations for each cell configuration are reported to clearly illustrate the variability observed in the results. Notably, only a small deviation was detected during the three-point bending tests, which suggests that the samples exhibit a high level of processing quality. Such minimal variation in the data indicates consistent manufacturing, as significant deviations would typically point to flaws or inconsistencies in the material structure. Therefore, the observed results reinforce the reliability of the production process and the overall integrity of the tested samples.

Fig. 8 shows the fracture of the panels that underwent bending tests. It can be observed how the fracture easily propagates within the C4 sandwich panels, while the C2 cells offer a more significant obstacle to the fracture to propagate.

Moreover, while in the C4 lattice sandwich panels it is possible to notice a straighter and more vertical path for the fracture propagation, for the C2 panels the fracture propagation path deviates from the vertical direction. In both cases, following the failure of the skin, the fracture rapidly propagates in the core lattice until the complete failure of the specimen.

To further understand the failure mechanism from a microscopic perspective, a fractographic analysis has been performed on a representative sample. Localized plastic deformation is observed in the skin region, as evidenced by the presence of dimples (Fig. 9), indicative of a ductile fracture mechanism governed by microvoid nucleation and coalescence. However, the simultaneous presence of cleavage surfaces suggests a transition from ductile crack initiation to rapid, brittle propagation. Macroscale examination further highlights a smoother, more reflective fracture surface in the strut regions, which indicates a brittle fracture. These results indicate that, despite some marginal ductile features in the skin area, the overall fracture behavior of the lattice sandwich panel is predominantly brittle.

4.2. Numerical results

The force–displacement curves of the two-dimensional equivalent numerical models for the Three-Point Bending (TPB) are presented in Fig. 10 and Fig. 11 for the three configurations with unit cell length $L = 2$ mm (C2) and the three configurations with unit cell length $L = 4$ mm (C4), respectively. The same figures show the corresponding experimentally measured force–displacement curve for each numerical simulation.

A comparison of numerical and experimental curves shows a good agreement between the simulation and experimental results for all the manufactured lattice specimen configurations: the numerical model effectively captures the primary brittle failure behavior of the sandwich lattice, as evidenced by the abrupt loss of stiffness after the first significant load drop. All the simulations are halted at the first significant load drop, which coincides with the skin failure.

The predicted distributions of the damage variable ω corresponding to the load drop step are shown in Figs. 12 and 13 for the three virtual specimens with $L = 2$ mm (C2) and the three virtual specimens with $L = 4$ mm (C4), respectively. The damage distribution maps are superimposed on the predicted deformed configuration at the same time step. A value of ω nearing 1 indicates that the material's stiffness approaches zero, signifying that the material has failed. In all tested specimen configurations, the initial critical damage is localized in a region of the model associated with the inferior skin. Some of the earlier figures also show the computed initial propagation path, defined as the line connecting the initial critical damage in the skin to the consecutive (simulation-time-wise) localized zones where the damage variable ω reaches its maximum value.

5. Discussion

The comparison between the numerical and experimental results demonstrates that the two-dimensional equivalent numerical model successfully simulates the mechanical behavior of the lattice sandwich structure.

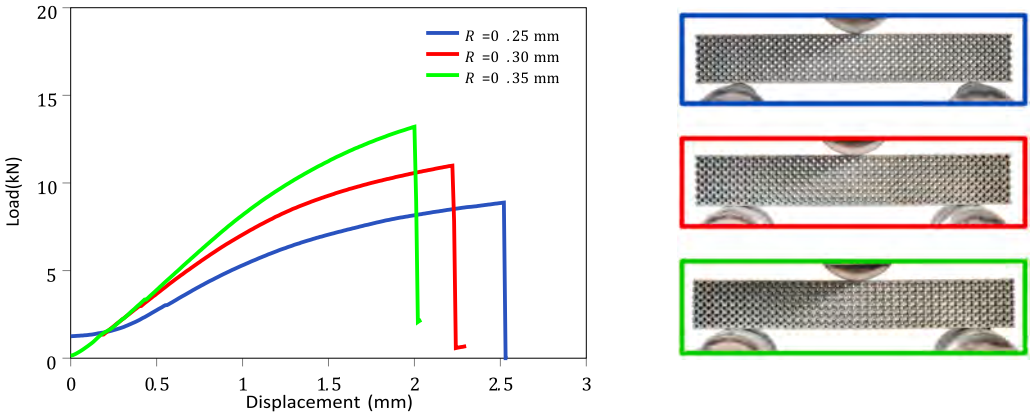

Fig. 6. Experimental results from three-point bending (TPB) tests for the specimen with C2 unit cells by varying the beam radius (R).

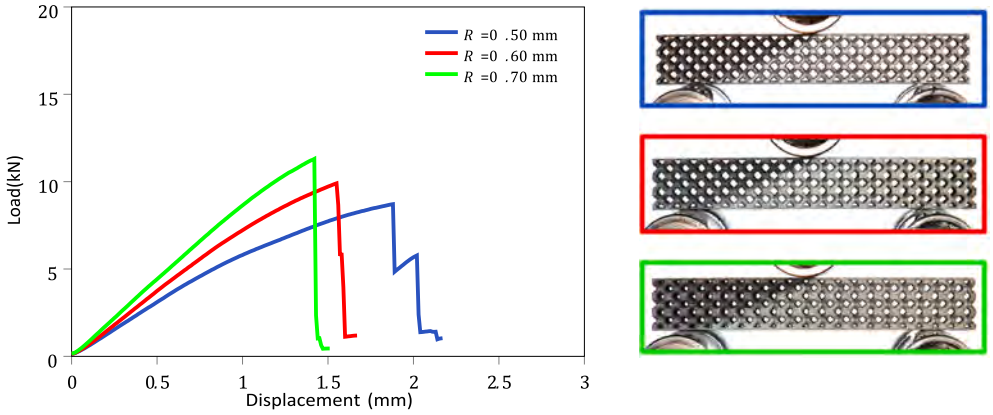

Fig. 7. Experimental results from three-point bending (TPB) tests for the specimen with C4 unit cells by varying the beam radius (R).

Table 6
Mean value and standard deviation from three-point bending tests results in terms of force and displacements.

	Force [N]		Displacements [mm]	
	mean	st.dev.	mean	st.dev.
C2-R0.25	8613,75	±280,29	2,44	±0,39
C2-R0.30	11637,08	±386,25	2,23	±0,28
C2-R0.35	13409,17	±335,39	2,00	±0,25
C4-R0.50	8608,13	±103,13	1,89	±0,02
C4-R0.60	9564,38	±350,63	1,48	±0,08
C4-R0.70	11056,88	±256,88	1,26	±0,16

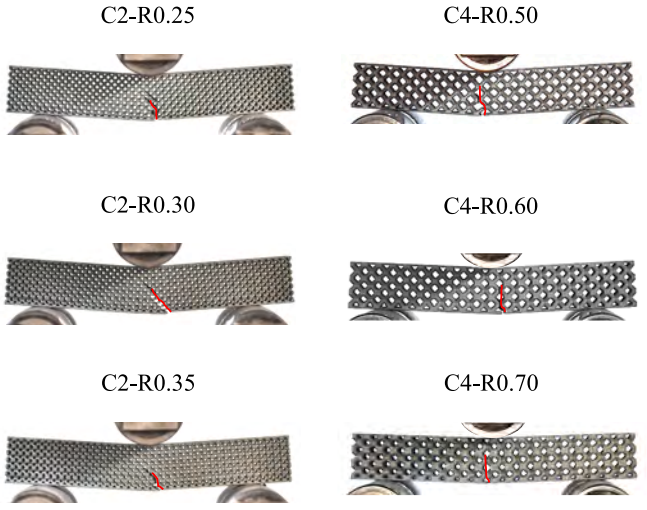

Fig. 8. Images of the fractured samples during three-point bending tests, the crack path propagation is highlighted with a red line. (For interpretation of the references to colour in this figure legend, the reader is referred to the web version of this article.)

An examination of the experimental and numerical load–displacement curves shows that the two-dimensional model accurately predicts both the load-absorbing capacity of the sandwich structure, and the primary brittle failure mode associated with skin failure. The simulation curves for all tested configurations, shown in Fig. 10 and Fig. 11, closely match the experimental curves in the elastic region. In the initial part of the non-linear region, the computed total reaction force measured at the point of application of the enforced displacement exceeds the values observed in the experiments. This discrepancy can be attributed to the adopted continuum damage mechanics approach, which does not account for plastic effects. Nevertheless, the numerical model successfully captures the primary brittle failure behavior of the sandwich lattice, as evidenced by the abrupt loss of stiffness after the first significant load drop.

Additionally, the numerical results are consistent with the experimental observations regarding the localization of critical skin damage and the propagation path within the core lattice. The numerical model successfully predicts the localization of the critical skin damage observed during the experimental tests, as illustrated in Fig. 14, for the C4-050 specimen.

A comparison of the damage distribution maps in Figs. 12 and 13 with the images of the fractured samples shown in Fig. 8 demonstrates that in most of the analyzed cases, the numerical results can predict the direction of the initial propagation path inside the core lattice. The empirical relations based on the Gibson and Ashby model (Gibson, 2003) are often employed to predict the yield stress and elastic modulus capabilities of metal lattice structures. According to this model, the mechanical properties of a lattice unit cell are power relations of the volume fraction (or relative density) of the lattice material. The two-dimensional numerical model's geometry was established based on a preliminary assessment of the bending stiffness of the two-dimensional representation of the BCC lattice compared to its actual three-dimensional structure. However, since volume fraction is a geometric property that significantly influences the behavior of a lattice material, it is worth comparing this quantity between the three-dimensional and the two-dimensional topology. The aspect ratio λ is defined as

$$\lambda = \frac{t}{L} \tag{19}$$

where L is the unit cell length and t is twice the radius R of a beam of a BBC unit cell or the thickness of a wall of the square honeycomb lattice unit cell. By interpolating the data in (Stumme et al., 2023), is it possible to obtain a polynomial expression for the volume fraction of the BCC unit cell

$$V_{f,3D} = p_1\lambda^5 + p_2\lambda^4 + p_3\lambda^3 + p_4\lambda^2 + p_5\lambda + p_6 \tag{20}$$

where $p_1 = 7.33$, $p_2 = -13.26$, $p_3 = 3.732$, $p_4 = 2.958$, $p_5 = 0.2948$, $p_6 = -0.008759$. From simple geometric consideration, the expression for the area of the square honeycomb unit cell reads

$$A = 2t\left(L\sqrt{2} - t\right) \tag{21}$$

The corresponding volume fraction $V_{f,2D}$ is obtained by dividing Eq. (5) by the square of the unit cell length

$$V_{f,2D} = \frac{A}{L^2} = 2\sqrt{2}\lambda - 2\lambda^2 \tag{22}$$

Both $V_{f,3D}$ and $V_{f,2D}$ as a function of the aspect ratio λ are shown in Fig. 15.

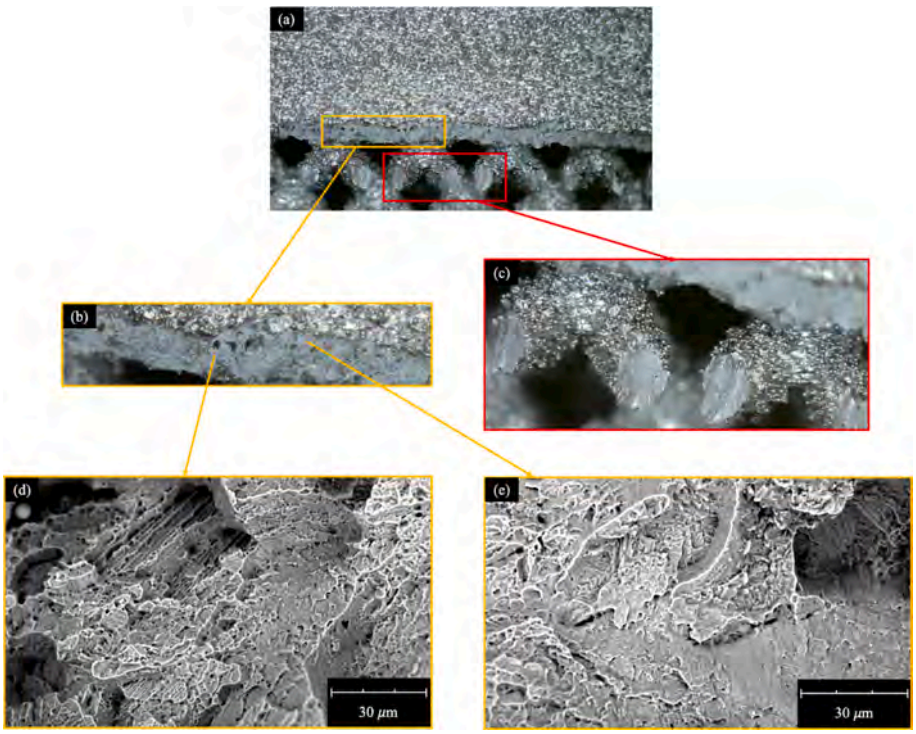

Fig. 9. Fractography analysis of C2-R0.30 sample after three-point bending tests. (a) macroscopic images of the fractured lattice sandwich panels; (b) detail of the fracture surface in correspondence with the skin; (c) detail of the fracture surface in correspondence with the struts; (d) end (e) SEM analysis of the skin area, where dimples and cleavage surfaces can be observed.

Additionally, a volume fraction ratio (VFR) parameter can be defined as the ratio of the volume fraction of the virtual specimens ($V_{f,2D}$) to the volume fractions of the manufactured specimens ($V_{f,3D}$). From Fig. 16, where the volume fraction ratio is plotted against the aspect ratio λ, it is possible to notice that, for most of the configurations that have been considered, the VFR values are within the range 0.6–0.8. This result can be used in further studies to determine an initial geometry of numerical two-dimensional models of lattice sandwich structures with similar lattice core topology.

The aim of the current study is to develop and validate a *macroscopic*, two-dimensional equivalent numerical model to predict the overall mechanical response and failure behavior of the metal lattice sandwich panels, and the experimental analysis also focused on macroscopic observations, such as load–displacement curves and visual crack propagation paths.

The isotropic damage model has been selected for its computational efficiency and ability to capture primary macroscopic failure modes. However, Ti-6Al-4V components fabricated via L-PBF can exhibit anisotropy in their microstructure, mechanical properties, and fracture behaviors. Similarly, lattice geometries with structural anisotropies can exhibit directional characteristics in their failure behavior. Although anisotropic or oriented damage models would be more accurate for such scenarios, where a more detailed representation of failure mechanisms is required, for the sake of simplicity, the assumption of isotropic failure was made.

The numerical model adopts a damage formulation without plasticity, assuming a primarily brittle failure mode. This assumption is supported by experimental evidence obtained from the three-point bending tests, which consistently showed abrupt fracture in all tested specimens, including those with higher volume fractions (e.g., C2-R0.35 and C4-R0.70). The load–displacement curves (Figs. 6 and 7) show a sudden load drop, with minimal or no indication of plastic behavior. Visual inspection of the fractured specimens (Fig. 8) confirmed that failure initiates in the lower skin of the sandwich panels and rapidly propagates through the core, indicating that structural collapse is triggered by brittle fracture of the skin. Further support to the adopted damage formulation for the numerical experiments is obtained from the fractographic analysis discussed in Section 4.1, which shows that the overall fracture behavior of the lattice sandwich panel is predominantly brittle. All these combined findings justify the use of a purely brittle damage model and indicate that, for the tested Ti-6Al-4V lattice sandwich panels manufactured by L-PBF, plastic deformation does not play a significant role in the failure process of this specific sandwich panel configuration, even at higher densities.

In discussing the computational cost of the proposed approach, it is worth noting that using a computational model based on the Virtual Element Method offers a unique advantage over the standard Finite Element Method of handling elements with an arbitrary number of nodes. This feature enabled localized mesh refinement in the region of interest, i.e. where crack propagation is expected. Consequently, this streamlined the mesh generation process and reduced the degrees of freedom in the non-linear analysis by confining the mesh refinement to a specific zone. The CPU time needed for static analysis generally is a quadratic or cubic function of the number of degrees of freedom in the computational model (Senthilkumar and Element, 2002). This number of degrees of freedom, in turn, is a function of the quantity and types of elements in the model.

To evaluate the impact of the local mesh refinement strategy on computational cost, a comparison can be made between the number of DOFs for a representative virtual specimen modeled with both a locally refined mesh and a uniformly fine mesh that maintains equivalent resolution in the critical region. The uniform mesh required approximately three times more DOFs to achieve similar resolution across the entire domain, resulting in a corresponding increase in memory usage and CPU time. For example, in the case of the C4-R0.60 specimen, the locally refined mesh used 29,416 DOFs, while a uniformly fine mesh would have required 100,500 DOFs. This demonstrates that the VEM-based local mesh refinement strategy effectively concentrates computational effort only where it is needed.

In order to assess the computational efficiency of the proposed

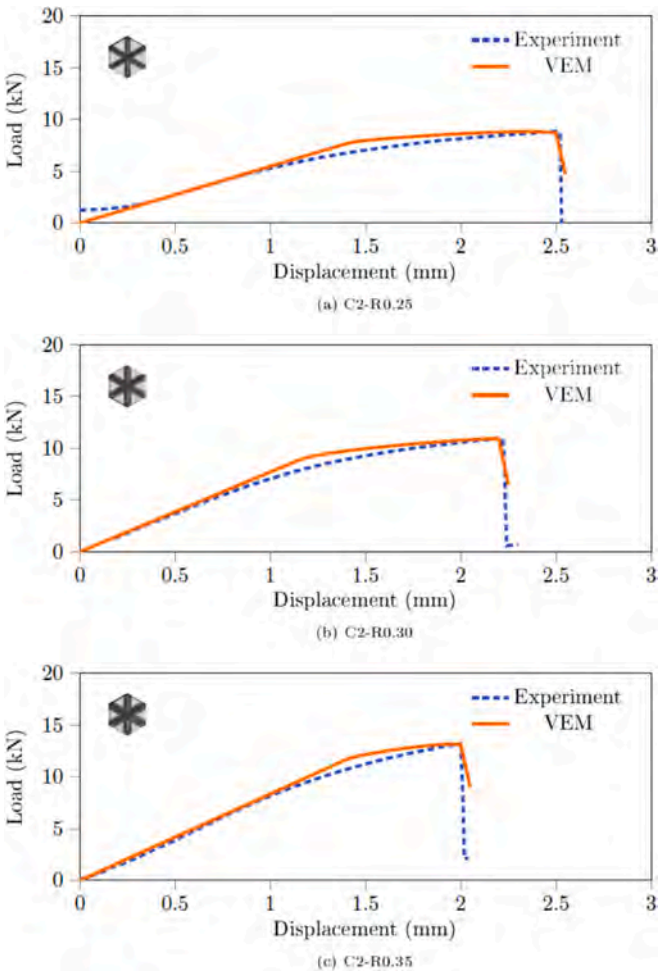

Fig. 10. Three-Point Bending (TPB) test experimental and two-dimensional numerical results comparison for the BCC unit cell with length $L = 2$ mm: (a) three-dimensional unit cell with $R = 0.25$ mm ($V_{f,3D} = 0.264$) against two-dimensional unit cell with $R_e = 0.070$ mm ($V_{f,2D} = 0.188$); (b) three-dimensional unit cell with $R = 0.30$ mm ($V_{f,3D} = 0.358$) against numerical two-dimensional unit cell with $R_e = 0.095$ mm ($V_{f,2D} = 0.251$); (c) three-dimensional unit cell with $R = 0.35$ mm ($V_{f,3D} = 0.457$) against two-dimensional unit cell with $R_e = 0.105$ mm ($V_{f,2D} = 0.275$).

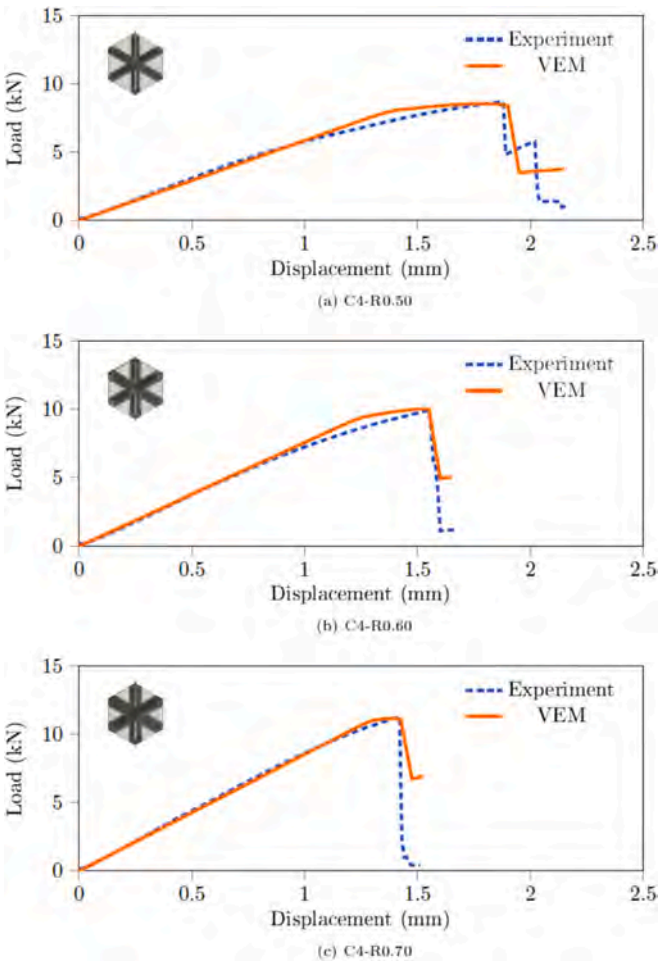

Fig. 11. Three-Point Bending (TPB) test experimental and two-dimensional numerical results comparison for the BCC unit cell with length $L = 4$ mm: (a) three-dimensional unit cell with $R = 0.50$ mm ($V_{f,3D} = 0.264$) against two-dimensional unit cell with $R_e = 0.15$ mm ($V_{f,2D} = 0.201$); (b) three-dimensional unit cell with $R = 0.60$ mm ($V_{f,3D} = 0.358$) against numerical two-dimensional unit cell with $R_e = 0.20$ mm ($V_{f,2D} = 0.263$); (c) three-dimensional unit cell with $R = 0.70$ mm ($V_{f,3D} = 0.457$) against two-dimensional unit cell with $R_e = 0.25$ mm ($V_{f,2D} = 0.322$).

equivalent two-dimensional modeling approach, a qualitative comparison is made with representative state-of-the-art three-dimensional finite element modeling approaches for metal BCC lattice materials found in the literature. This comparison aims to demonstrate the scale of computational savings achievable when modelling a single lattice unit cell by switching from a 3D FEM model to the proposed 2D VEM equivalent model. The selected examples represent well-established methodologies for conducting detailed 3D simulations of BCC lattice unit cells. They provide a relevant and reliable benchmark for assessing the relative efficiency of the proposed simplified 2D methodology. For instance, Alaimo et al. (Alaimo et al., 2023), who studied the compressive behavior of powder bed fusion manufactured BCC lattice structures, utilized 21,227 ANSYS Solid187 ten-node quadratic tetrahedral elements for the numerical model of a BCC unit cell with a volume fraction of 0.08. Kang et al. (Kang et al., 2019), in their study on topology optimization of metal lattice sandwich structures under bending loads, employed an average of 32,075 ANSYS Solid187 elements for meshing a unit cell having a volume fraction of 0.4. Guo2024 et al. (Guo et al., 2024) investigated the mechanical properties of LPBF AlSi10Mg BCC lattice structures using the GTN damage model. Their mesh convergence analysis indicated that 15,811 Abaqus's ten-node modified quadratic tetrahedron (C3D10M) elements were necessary to model a unit cell with a volume fraction of 0.18. Araghi et al. (Araghi et al., 2023), in their simulation of the compression test for AlSi10Mg BCC lattice structures using continuum damage mechanics, found that approximately 6400 Abaqus C3D10M ten-node tetrahedral quadratic elements were needed to mesh a unit cell with a volume fraction of 0.18 to ensure the convergence of the simulation results. In contrast, the proposed equivalent two-dimensional approach utilized a maximum of 2898 polygonal elements to mesh the unit cell of the model with $V_{f,2D} = 0.263$, which corresponds to a three-dimensional volume fraction $V_{f,3D} = 0.358$.

While direct comparisons of CPU times across different studies are often impractical due to variations in computational hardware, software implementations, and specific problem setups, the number of elements and the resulting degrees of freedom in a computational model can serve as robust and widely accepted measures for assessing computational cost. As previously mentioned, the CPU time required for static analysis typically scales as a quadratic or cubic function of the total number of degrees of freedom in the computational model. The number of degrees of freedom, in turn, is directly proportional to the quantity and type of elements used for discretization. Therefore, a significant reduction in the number of elements directly translates to a substantial reduction in DOFs and, consequently, a notable decrease in CPU time. While the volume

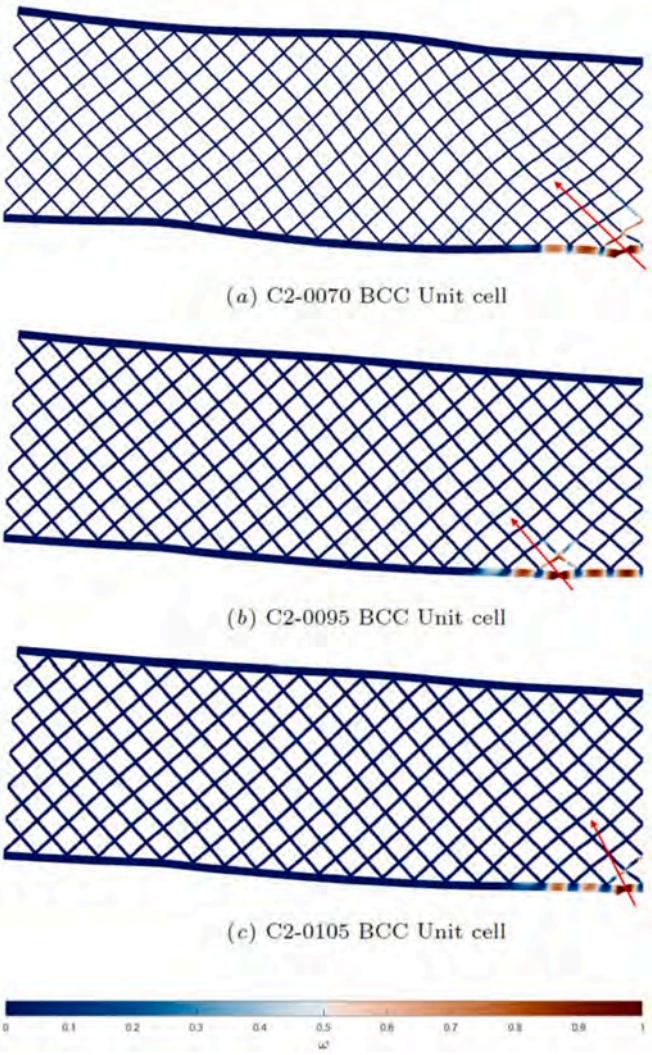

Fig. 12. Predicted damage distribution maps at the critical load and initial propagation path for the three virtual specimens with $L = 2$ mm and (a) $R_e = 0.070$ mm, (b) $R_e = 0.095$ mm, (c) $R_e = 0.105$ mm.

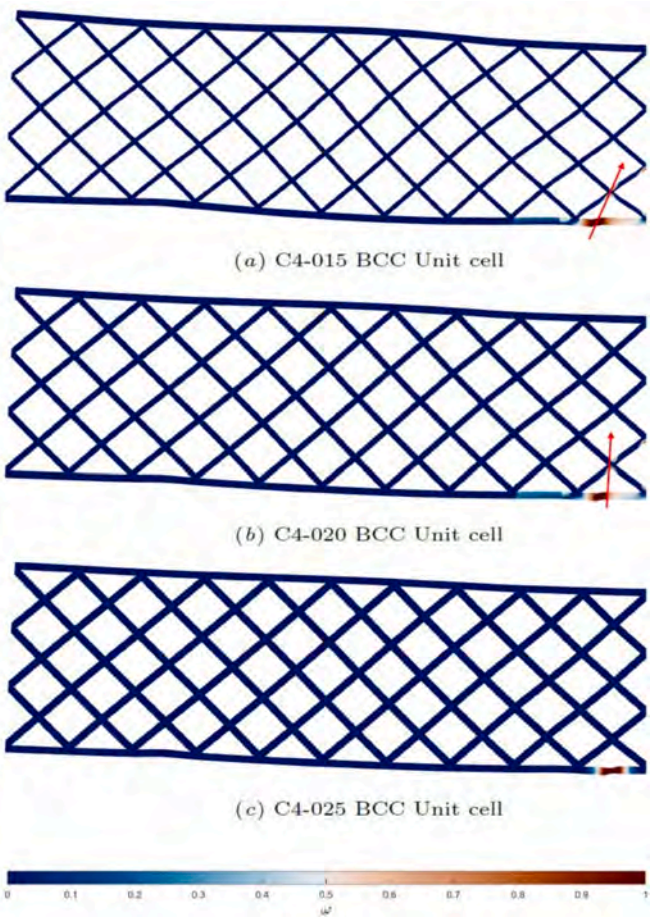

Fig. 13. Predicted damage distribution maps at the critical load and initial propagation path for the three virtual specimens with $L = 4$ mm and (a) $R_e = 0.15$ mm, (b) $R_e = 0.20$ mm, (c) $R_e = 0.25$ mm.

fractions of the compared models differ, this comparison remains highly pertinent as it demonstrates the inherent efficiency of the proposed approach. Specifically, the 2D model utilizes a maximum of 2898 polygonal elements for a unit cell corresponding to a three-dimensional volume fraction $V_{f,3D}$ of 0.358. This element count is significantly lower than that reported for any of the cited 3D FEM models, even those with considerably lower volume fractions. This highlights that the efficiency gain is not merely a function of volume fraction but is intrinsic to the dimensional reduction of the analyses. The summary of this comparison is presented in Table 7 and demonstrates that the proposed method significantly reduces computational costs compared to three-dimensional finite element modeling while still producing results consistent with experimental observations.

Regarding the mechanical behavior of lattice sandwich panels, it can be observed how increasing the beam radius increases the stiffness of the lattice sandwich panels. This held true for C2 and C4 lattice sandwich panels due to increased volume fraction (Figs. 6 and 7). Instead, by considering samples with the same volume fraction, it is possible to observe how the C2 cell allows higher loads and displacements. These findings suggest a significant influence of the number of cells per unit area on the mechanical responses from the sandwich panel. In detail, a lattice core with a higher number of unit cells facilitates the deformation of the entire structure, improving its strength. This can be explained by considering the number of struts withstanding the applied force. As a matter of fact, by taking into account a core lattice volume of 80 mm × 12 mm × 12 mm, C2 (2 mm × 2 mm × 2 mm) and C4 (4 mm × 4 mm × 4 mm) will result in 1440 and 180 cells, respectively. This means C2 specimens present a number of unit cells 8 times higher than C4 for each volume fraction. Overall, by fixed volume fraction, it arises that a better distribution of loads and displacement can be obtained using a dense core with a higher number of unit cells per unit area. The numerical simulation allows to better understand the above-mentioned experimental observations. Fig. 17 shows the equivalent strain distribution for C2-R0.25 and C4-R0.50 lattice sandwich panels designed with the same volume fraction equal to 0.264 (see Table 1). The comparison with the respective equivalent two-dimensional model shows that for C2-R0.25, there is a better distribution of the equivalent strain along the skin. For C4-R0.50, instead, the core lattice structure cannot efficiently distribute the equivalent strain, resulting in localization and premature skin failure.

6. Conclusions

In this study, an equivalent two-dimensional numerical model based on the non-linear Virtual Element Method (VEM) has been developed and validated to predict the mechanical response of Ti-6Al-4V BCC lattice sandwich panels manufactured by L-PBF and subjected to bending loads. Based on the results obtained, the following main conclusions can be drawn:

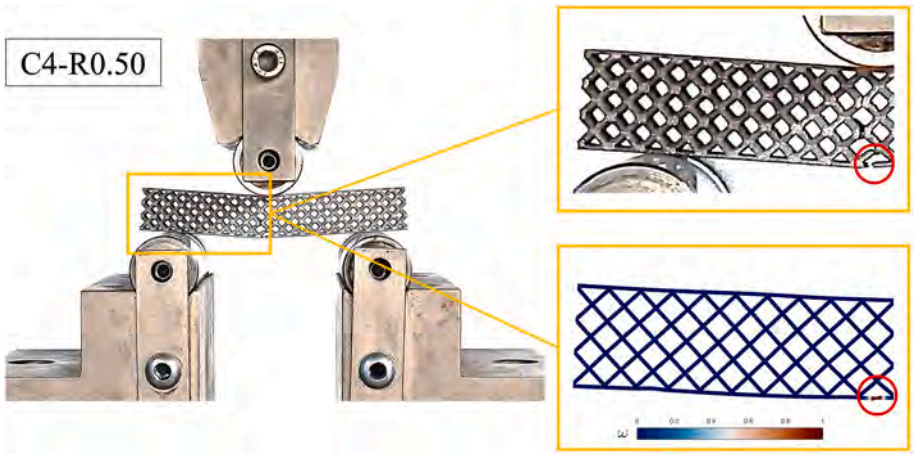

Fig. 14. Localization of the critical skin damage: (a) experimental test of the C4-R0.50 specimen (b) numerical result (damage distribution) for the equivalent two-dimensional model with $L = 4$ mm and $R_e = 0.15$ mm. The red circles highlight the starting point of the lattice sandwich panel failure. (For interpretation of the references to colour in this figure legend, the reader is referred to the web version of this article.)

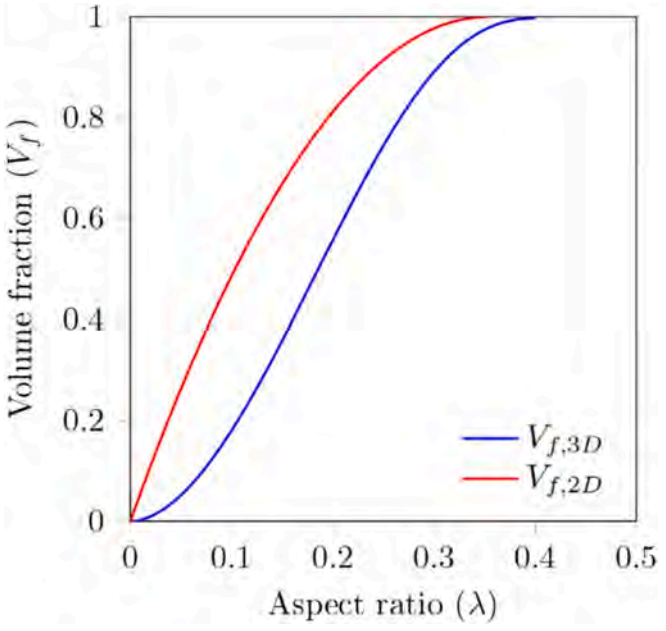

Fig. 15. Plot of volume fraction (V_f) as a function of the aspect ratio (λ) for the BCC unit cell ($V_{f,3D}$) and its two-dimensional projection ($V_{f,2D}$).

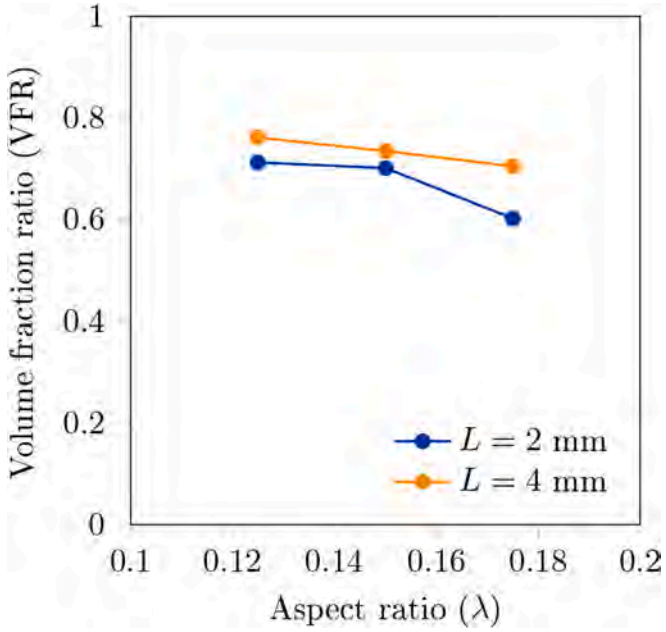

Fig. 16. Volume fraction ratio (VFR) as a function of the aspect ratio (λ).

1. The established criterion, based on comparing the bending stiffness of three-dimensional and two-dimensional BCC lattice unit cells, has proven to effectively determine the initial geometry of the two-dimensional virtual specimens with adequate reliability.
2. The numerical results are in substantial agreement with the experimental observations, proving that the VEM-based two-dimensional model accurately predicts the load-bearing capacity of the lattice core sandwich panel, the primary brittle failure mode associated with skin failure, and the localization of the critical skin damage.
3. The proposed two-dimensional approach significantly reduces the number of elements required for analyses, resulting in reduced CPU time compared to three-dimensional FEM approaches. This efficiency is attributed to the inherent model's dimensional reduction from 3D to 2D, as well as the Virtual Element Method's ability to generate localized and confined mesh refinements.
4. The values obtained for the volume fraction ratio (VFR) can be valuable for future studies to determine the initial geometry of equivalent two-dimensional models of lattice sandwich structures with similar lattice core topologies.
5. The stiffness of the lattice sandwich panels is mainly affected by the beam radius, which increases the aspect ratio and the volume fraction.
6. The number of unit cells per unit area is an important factor to consider in the design phase of AM lattice sandwich panels due to its

Table 7
Number and type of mesh elements used for the numerical model of a single BCC unit cell.

Reference	V_f	Element Type	No. of Elements
Alaimo et al. (2023)	0.08	3D quadratic tetrahedral	21,227
Kang et al. (2019)	0.4	3D quadratic tetrahedral	32,075
Guo et al. (2024)	0.18	3D quadratic tetrahedral	15,811
Araghi et al. (2023)	0.18	3D quadratic tetrahedral	6400
Present approach	0.358*	2D linear polygonal	2898

* Volume fraction of the simulated 3D specimen.

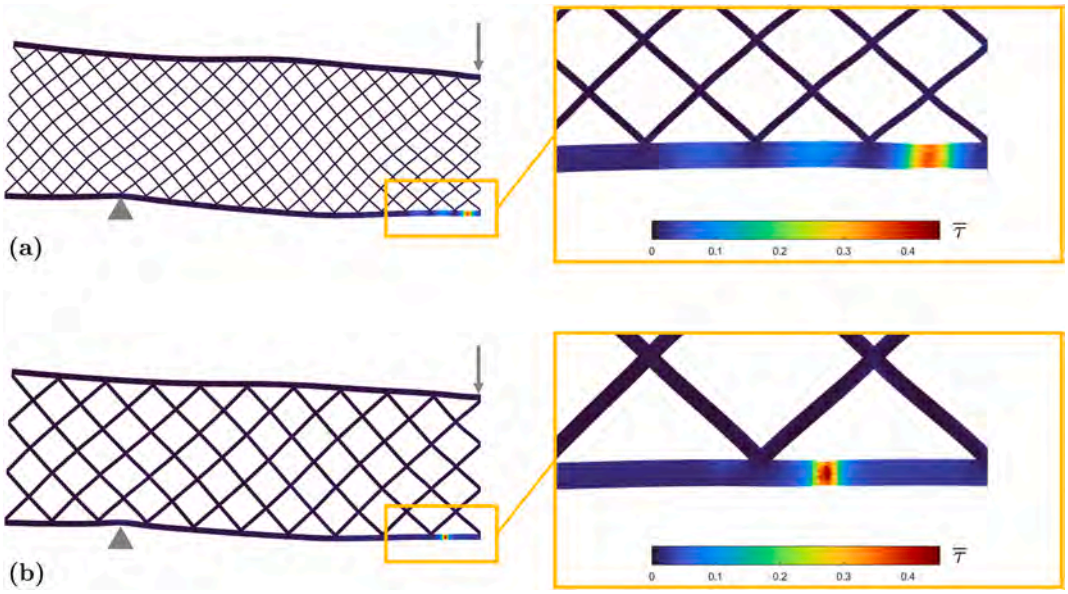

Fig. 17. Virtual element predictions of equivalent strain (τ) distributions within the sandwich lattice model of (a) sample with $L = 2$ mm and $R_e = 0.070$ mm, equivalent to specimen C2-R0.25 and (b) sample with $L = 4$ mm and $R_e = 0.15$ mm, equivalent to specimen C4-R0.50.

effect on the distribution of the stress/strain along the skin, significantly impacting the mechanical resistance of the structure.

The numerical model presented in this study provides a time-effective design tool for selecting the optimal geometrical features that enhance the mechanical performance of BCC lattice sandwich panels subjected to bending loads. The purpose of this work is to establish and validate the proposed numerical approach and the Ti-6Al-4V BCC lattice core was selected due to its relatively simple geometry, established manufacturing feasibility via L-PBF, and frequent adoption in aerospace applications. The proposed method can potentially be extended to other types of periodic lattice topologies. The primary requirement for such an extension is the definition of an appropriate equivalent two-dimensional representation that captures the predominant mechanical behavior of the original three-dimensional lattice. However, as more complex lattice core topologies and different parent materials may influence the performance of the proposed approach, future work will explore the application to other unit cell topologies and materials in order to evaluate its robustness.

CRediT authorship contribution statement

Marco Lo Cascio: Writing – original draft, Validation, Software, Methodology, Data curation. **Gaetano Pollara:** Writing – original draft, Validation, Methodology, Investigation, Data curation, Conceptualization. **Dina Palmeri:** Formal analysis, Conceptualization. **Gianluca Buffa:** Writing – review & editing, Supervision, Conceptualization. **Alberto Milazzo:** Supervision, Project administration. **Livan Fratini:** Supervision, Project administration, Conceptualization.

Declaration of competing interest

The authors declare that they have no known competing financial interests or personal relationships that could have appeared to influence the work reported in this paper.

Acknowledgements

This study was carried out within the MICS (Made in Italy – Circular and Sustainable) Extended Partnership and received funding from the European Union Next-Generation EU (PIANO NAZIONALE DI RIPRESA E RESILIENZA (PNRR) – MISSIONE 4 COMPONENTE 2, INVESTIMENTO 1.3 – D.D. 1551.11–10-2022, PE00000004). This manuscript reflects only the authors' views and opinions, neither the European Union nor the European Commission can be considered responsible for them.

Data availability

Data will be made available on request.

References

Acanfora, V., Saputo, S., Russo, A., Riccio, A., 2021. A feasibility study on additive manufactured hybrid metal/composite shock absorbers. Compos. Struct. 268, 113958. https://doi.org/10.1016/j.compstruct.2021.113958.

Alaimo, A., Del Prete, A., Mantegna, G., Orlando, C., Panella, F.W., Primo, T., Tumino, D., Vindigni, C.R., 2023. Modified beam modeling of powder bed fusion manufactured lattice structures. Int. J. Mech. Sci. 259, 108599. https://doi.org/10.1016/j.ijmecsci.2023.108599.

Al-Ketan, O., Rowshan, R., Abu Al-Rub, R.K., 2018. Topology-mechanical property relationship of 3D printed strut, skeletal, and sheet based periodic metallic cellular materials. Addit. Manuf. 19, 167–183. https://doi.org/10.1016/j.addma.2017.12.006.

Araghi, M., Rokhgireh, H., Nayebi, A., 2023. Experimental and FEM investigation of BCC lattice structure under compression test by using continuum damage mechanics with micro-defect closure effect. Mater. Des. 232, 112125. https://doi.org/10.1016/j.matdes.2023.112125.

Ashby, M.F., 2006. The properties of foams and lattices. Philos. Trans. R. Soc. A Math. Phys. Eng. Sci. 364, 15–30. https://doi.org/10.1098/rsta.2005.1678.

Astm, A., 2014. E290-14 Standard Test Methods for Bend Testing of Material for Ductility. ASTM International, West Conshohocken, PA https://www.astm.org/ (accessed June 11, 2025.

Bartsch, K., Herzog, D., Bossen, B., Emmelmann, C., 2021. Material modeling of Ti–6Al–4V alloy processed by laser powder bed fusion for application in macro-scale process simulation. Mater. Sci. Eng. A 814, 141237. https://doi.org/10.1016/j.msea.2021.141237.

Beirão Da Veiga, L., Brezzi, F., Cangiani, A., Manzini, G., Marini, L.D., Russo, A., 2013. Basic principles of virtual element methods. Math. Models Methods Appl. Sci. 23, 199–214. https://doi.org/10.1142/S0218202512500492.

Benedetti, M., du Plessis, A., Ritchie, R.O., Dallago, M., Razavi, N., Berto, F., 2021. Architected cellular materials: a review on their mechanical properties towards fatigue-tolerant design and fabrication. Mater. Sci. Eng. R. Rep. 144, 100606. https://doi.org/10.1016/j.mser.2021.100606.

Bici, M., Brischetto, S., Campana, F., Ferro, C.G., Seclì, C., Varetti, S., Maggiore, P., Mazza, A., 2018. Development of a multifunctional panel for aerospace use through SLM additive manufacturing. Procedia CIRP 67, 215–220. https://doi.org/10.1016/j.procir.2017.12.202.

Blakey-Milner, B., Gradl, P., Snedden, G., Brooks, M., Pitot, J., Lopez, E., Leary, M., Berto, F., du Plessis, A., 2021. Metal additive manufacturing in aerospace: a review. Mater. Des. 209, 110008. https://doi.org/10.1016/j.matdes.2021.110008.

Böhm, C., Munk, L., Hudobivnik, B., Aldakheel, F., Korelc, J., Wriggers, P., 2023. Virtual elements for computational anisotropic crystal plasticity. Comput. Methods Appl. Mech. Eng. 405, 115835. https://doi.org/10.1016/j.cma.2022.115835.

Buffa, G., Palmeri, D., Pollara, G., Di Franco, F., Santamaria, M., Fratini, L., 2024. Process parameters and surface treatment effects on the mechanical and corrosion resistance properties of Ti6Al4V components produced by laser powder bed fusion. Prog. Addit. Manuf. 9, 151–167. https://doi.org/10.1007/s40964-023-00440-9.

Červinek, O., Pettermann, H., Todt, M., Koutný, D., Vaverka, O., 2022. Non-linear dynamic finite element analysis of micro-strut lattice structures made by laser powder bed fusion. J. Mater. Res. Technol. 18, 3684–3699. https://doi.org/10.1016/j.jmrt.2022.04.051.

da Veiga, L.B., Brezzi, F., Marini, L.D., 2013. Virtual elements for linear elasticity problems. SIAM J. Numer. Anal. 51, 794–812. https://doi.org/10.1137/120874746.

de Vree, J.H.P., Brekelmans, W.A.M., van Gils, M.A.J., 1995. Comparison of nonlocal approaches in continuum damage mechanics. Comput. Struct. 55, 581–588. https://doi.org/10.1016/0045-7949(94)00501-S.

DebRoy, T., Wei, H.L., Zuback, J.S., Mukherjee, T., Elmer, J.W., Milewski, J.O., Beese, A. M., Wilson-Heid, A., De, A., Zhang, W., 2018. Additive manufacturing of metallic components – Process, structure and properties. Prog. Mater Sci. 92, 112–224. https://doi.org/10.1016/j.pmatsci.2017.10.001.

Deshpande, V.S., Ashby, M.F., Fleck, N.A., 2001. Foam topology: bending versus stretching dominated architectures. Acta Mater. 49, 1035–1040. https://doi.org/10.1016/S1359-6454(00)00379-7.

Georges, H., Großmann, A., Mittelstedt, C., Becker, W., 2022. Structural modeling of sandwich panels with additively manufactured strut-based lattice cores. Addit. Manuf. 55. https://doi.org/10.1016/j.addma.2022.102788.

Gibson, L.J., 2003. Cellular solids. MRS Bull. 28, 270–274. https://doi.org/10.1557/mrs2003.79.

Gibson, L.J., Ashby, M.F., 1997. Cellular Solids. Cambridge University Press, 10.1017/CBO9781139878326.

Guo, H., Wang, H., Li, X., Dong, Z., Zhang, L., Li, W., 2024. Investigation of mechanical properties of laser powder bed fused AlSi10Mg lattice structures using GTN damage model. J. Mater. Res. Technol. 29, 1937–1948. https://doi.org/10.1016/j.jmrt.2024.01.187.

Imbalzano, G., Tran, P., Ngo, T.D., Lee, P.V., 2017. Three-dimensional modelling of auxetic sandwich panels for localised impact resistance. J. Sandw. Struct. Mater. 19, 291–316. https://doi.org/10.1177/1099636215618539.

Jirásek, M., 2007. Nonlocal damage mechanics. Revue Européenne De Génie Civil 11, 993–1021. https://doi.org/10.3166/regc.11.993-1021.

Kang, D., Park, S., Son, Y., Yeon, S., Kim, S.H., Kim, I., 2019. Multi-lattice inner structures for high-strength and light-weight in metal selective laser melting process. Mater. Des. 175, 107786. https://doi.org/10.1016/j.matdes.2019.107786.

Li, C., Lei, H., Liu, Y., Zhang, X., Xiong, J., Zhou, H., Fang, D., 2018. Crushing behavior of multi-layer metal lattice panel fabricated by selective laser melting. Int. J. Mech. Sci. 145, 389–399. https://doi.org/10.1016/j.ijmecsci.2018.07.029.

Li, X., Lu, Z., Yang, Z., Yang, C., 2018. Anisotropic in-plane mechanical behavior of square honeycombs under off-axis loading. Mater. Des. 158, 88–97. https://doi.org/10.1016/j.matdes.2018.08.007.

Lo Cascio, M., Milazzo, A., Benedetti, I., 2019. Virtual element method: micro-mechanics applications. Key Eng. Mater. 827, 128–133. https://doi.org/10.4028/www.scientific.net/KEM.827.128.

Lo Cascio, M., Milazzo, A., Benedetti, I., 2020. Virtual element method for computational homogenization of composite and heterogeneous materials. Compos. Struct. 232, 111523. https://doi.org/10.1016/j.compstruct.2019.111523.

Lo Cascio, M., Milazzo, A., Benedetti, I., 2021. A hybrid virtual–boundary element formulation for heterogeneous materials. Int. J. Mech. Sci. 199, 106404. https://doi.org/10.1016/j.ijmecsci.2021.106404.

Lozanovski, B., Leary, M., Tran, P., Shidid, D., Qian, M., Choong, P., Brandt, M., 2019. Computational modelling of strut defects in SLM manufactured lattice structures. Mater. Des. 171, 107671. https://doi.org/10.1016/j.matdes.2019.107671.

Luxner, M.H., Stampfl, J., Pettermann, H.E., 2005. Finite element modeling concepts and linear analyses of 3D regular open cell structures. J. Mater. Sci. 40, 5859–5866. https://doi.org/10.1007/s10853-005-5020-y.

Marino, M., Hudobivnik, B., Wriggers, P., 2019. Computational homogenization of polycrystalline materials with the virtual element method. Comput. Methods Appl. Mech. Eng. 355, 349–372. https://doi.org/10.1016/j.cma.2019.06.004.

Palmeri, D., Buffa, G., Pollara, G., Fratini, L., 2022. Sample building orientation effect on porosity and mechanical properties in Selective Laser Melting of Ti6Al4V titanium alloy. Mater. Sci. Eng. A 830, 142306. https://doi.org/10.1016/j.msea.2021.142306.

Palmeri, D., Pollara, G., Licari, R., Micari, F., 2023. Finite element method in L-PBF of Ti-6Al-4V: influence of laser power and scan speed on residual stress and part distortion. Metals (Basel) 13, 1907. https://doi.org/10.3390/met13111907.

Pijaudier-Cabot, G., Bažant, Z.P., 1987. Nonlocal damage theory. J. Eng. Mech. 113, 1512–1533. https://doi.org/10.1061/(ASCE)0733-9399(1987)113:10(1512).

Seiler, P.E., Tankasala, H.C., Fleck, N.A., 2019. The role of defects in dictating the strength of brittle honeycombs made by rapid prototyping. Acta Mater. 171, 190–200. https://doi.org/10.1016/j.actamat.2019.03.036.

M. Senthilkumar, The Finite Element Method: A Practical Course, 2002.

Simo, J.C., Ju, J.W., 1987. Strain- and stress-based continuum damage models—I. Formulation. Int. J. Solids Struct. 23, 821–840. https://doi.org/10.1016/0020-7683(87)90083-7.

Smith, M., Guan, Z., Cantwell, W.J., 2013. Finite element modelling of the compressive response of lattice structures manufactured using the selective laser melting technique. Int. J. Mech. Sci. 67, 28–41. https://doi.org/10.1016/j.ijmecsci.2012.12.004.

A. Stumme, M. Dorsey, A. Golding, S. Rudolph, Analysis of Bulk Dielectric Constant of Latticed Materials, 2023.

Vock, S., Klöden, B., Kirchner, A., Weißgärber, T., Kieback, B., 2019. Powders for powder bed fusion: a review. Prog. Addit. Manuf. 4, 383–397. https://doi.org/10.1007/s40964-019-00078-6.

Wei, K., Yang, Q., Yang, X., Tao, Y., Xie, H., Qu, Z., Fang, D., 2020. Mechanical analysis and modeling of metallic lattice sandwich additively fabricated by selective laser melting. Thin-Walled Struct. 146, 106189. https://doi.org/10.1016/j.tws.2019.106189.

Wei, Y., Zhang, C., Yuan, Y., Chen, P., Huang, C., Li, J., Yuan, M., 2023. Blast response of additive manufactured Ti–6Al–4V sandwich panels. Int. J. Impact Eng 176, 104553. https://doi.org/10.1016/j.ijimpeng.2023.104553.

Wu, Q., Gao, Y., Wei, X., Mousanezhad, D., Ma, L., Vaziri, A., Xiong, J., 2018. Mechanical properties and failure mechanisms of sandwich panels with ultra-lightweight three-dimensional hierarchical lattice cores. Int. J. Solids Struct. 132–133, 171–187. https://doi.org/10.1016/j.ijsolstr.2017.09.024.

Zhong, H., Song, T., Li, C., Das, R., Gu, J., Qian, M., 2023. The Gibson-Ashby model for additively manufactured metal lattice materials: its theoretical basis, limitations and new insights from remedies. Curr. Opin. Solid State Mater. Sci. 27, 101081. https://doi.org/10.1016/j.cossms.2023.101081.